



Transactions of the Canadian Society for Mechanical Engineering

Design of a Novel Deployable Mechanism for Capturing Tumbling Debris

| | |
|---|---|
| Journal: | <i>Transactions of the Canadian Society for Mechanical Engineering</i> |
| Manuscript ID | TCSME-2018-0146.R2 |
| Manuscript Type: | Article |
| Date Submitted by the Author: | 14-Oct-2018 |
| Complete List of Authors: | Li, XueAi; Harbin Institute of Technology, State Key Laboratory of Robotics and System Sun, Kui; Harbin Institute of Technology, State Key Laboratory of Robotics and System Liu, Hong; Harbin Institute of Technology, State Key Laboratory of Robotics and System |
| Keywords: | mechanism, deployable end-effector, capture, detumbling, active debris removal |
| Is the invited manuscript for consideration in a Special Issue? : | Not applicable (regular submission) |
| | |

SCHOLARONE™
Manuscripts

Design of a Novel Deployable Mechanism for Capturing Tumbling Debris

XueAi Li, Kui Sun* and Hong Liu

State Key Laboratory of Robotics and System, Harbin Institute of Technology, Harbin, China

* Corresponding Author: sunkui@hit.edu.cn

Draft

Abstract

The large number of man-made debris stemming for decades of space exploration threatens the safety of future space activities. It is therefore urgent to perform Active Debris Removal (ADR) missions to maintain the access to usable orbital space. This paper proposes a novel deployable end-effector and detumbling mechanism to capture tumbling debris. Three mechatronic subsystems for the capture, transmission, and actuation are highly integrated in the end-effector allowing for compact storage during space transport. Grippers composed of constant-torque hinges endow the mechanism with a deployable function and ensure a steady envelope by means of caging, without the need for precise tracking and complex control. With only one actuator, six grippers' simultaneous motion is implemented by arranging gears in a unique manner. Moreover, an optimal design of the grippers is performed to enlarge their envelope while reducing weight. A contact detumbling mechanism, composed of three dampers along three axes, is also provided based on revolute friction to slowdown the tumbling debris with residual angular momentum. Two slip rings are ingeniously embedded in each damper to transmit electricity considering signal interference and cable interwinding. Finally, simulations of the capturing and detumbling demonstrate the feasibility and effectiveness of the proposed mechanism.

Keywords: mechanism, deployable end-effector, capture, detumbling, active debris removal.

1. Introduction

Since the first launch of the Sputnik I, space exploration has been rapidly expanding with a great number of launches. Unfortunately, debris is produced in form of remnants from launches, collisions and malfunctions of spacecraft. Space debris is becoming a more and more significant threat to on-orbit activities. There are already more than 9000 earth-orbiting man-made objects (including many breakup fragments), with a combined mass exceeding 5 million kg (Liou et al. 2006). Several studies have indicated that the future stabilization of the orbital environment in the low earth orbit (LEO) requires the retrieval of 5 to 10 large debris objects per year (Wormnes et al. 2013).

The capturing phase plays a crucial role in the entire ADR mission, and one of the greatest challenges is capturing the target securely against sensor errors and control delays (Hirano et al. 2017). To deal with the problem, researchers are focusing on capture mechanisms in different approaches (Shan et al. 2016). Only the contact capturing methods including flexible methods and rigid methods are discussed in this paper, as a result of their reliabilities. ESA has sponsored the ROGER (Bischof 2003) program, whose end-effector can be either a net or a gripper. The net capturing and harpoons (Hausmann et al. 2015) are several concepts for the ADR mission proposed in the e.Deorbit project. A gecko adhesive gripper (Estrada et al. 2017) and dielectric elastomer minimum energy structures (Araromi et al. 2015) have also entered the public's awareness recently. Nonetheless, reliabilities and contact effects are insufficiently understood in these flexible methods, their acceptable tumbling limitations and stabilizing methods are expected as well. DLR has been also developing robotic technologies to capture a non-cooperative target in the DEOS (Reintsema et al. 2010). DRAPA has also studied the FRENDO project to perform the unaided capturing (Debus et al. 2009). Apparently, a manipulator with a specific gripper is a good choice to keep a rigid connection with a target. Nevertheless, it requires a specific grappling point and high-precision positioning between the end-effector and object, which may increase cost and weight dramatically. On the other hand, most of the proposed capture mechanisms occupy much precious room for the space transport.

Unfortunately, the residual angular momentum of tumbling debris brings great trouble for the capture. Various methods have been proposed on this problem to slowdown the tumbling. Some control algorithms requiring expensive sensors to obtain parameters for control have been proposed for detumbling in the rigid capturing methods (Aghili 2012; Zhang et al. 2017). Besides, JAXA has designed a brush-type contactor at the end of a manipulator for reducing the rotational rate of the target debris (Nishida et al. 2011). Matunaga et al. (2001) have proposed a contact/push-based control method using a cushion-type damper in order to absorb the rotational motion. Huang et al. (2016) adopted the adaptive postcapture backstepping control to detumble the debris through a tethered space robot. These methods could be classified into the contact detumbling methods, in which high-precision control is required. Additionally, some contactless detumbling methods have also been put forward to avoid collisions, including the thruster plume impingement (Nakajima et al. 2016), electrostatic method (Bennett et al. 2015), electromagnetic method (Gomez et al. 2017), ion beam irradiation (Kitamura et al. 2014), laser (Kumar et al. 2013) et al. However, it entails more complex equipment, increasing detumbling time and energy dissipation in the contactless methods. Compared to the contactless methods, the contact counterparts are able to generate larger detumbling forces, and thus are more effective.

A minimal size of the mechanism provides an alternative choice to facilitate the compaction for the storage during the space transport. The feature of the compact storage and the ability to be deployed into the service configuration of a large geometric volume make deployable mechanisms a perfect solution for the on-orbit activities. Researchers are devoted to investigating the deployable space mechanisms from reflector antennas to telescopes, radars and solar panels (Qi et al. 2016, 2017). The motivation of this paper is to develop a deployable end-effector and detumbling mechanism to capture tumbling debris targets. Three mechatronic subsystems for the capture, transmission, and actuation are highly integrated in the end-effector. “Caging” is adopted to grasp the object without precise positioning that uses complex feedback control (Hirano et al. 2013). The application of constant-torque hinges (Mcguire et al. 2006) allows for the compact storage during the space transport. Mechanism is arranged in a unique manner to ensure a secure grasp. To enlarge the envelope and to reduce the weight of the end-effector, grippers are

optimized based on the caging grasp and kinematic synthesis. In addition, a contact detumbling method without high-precision control or a complex mechanism is proposed. A passive detumbling mechanism based on the friction principle is designed to consume the residual angular momentum around three axes. Three dampers in the detumbling mechanism are arranged according to the tumbling of debris. Assembly mechanisms are also designed to connect the dampers, considering the compaction and noninterference. For the simplicity of each damper, the detumbling torque generated by two revolute friction disks does negative work to slowdown the target. In case of the signal interference and cable interwinding during the rotation, two slip rings are embedded in each damper to transmit signals. At last, the performance of the proposed mechanism is verified in virtual simulation software.

This paper highlights the design of a novel deployable mechanism for capturing the tumbling debris. Contributions of this study are: i) a novel concept addressing the drawbacks of both the flexible capturing methods and rigid methods in a traditional manner. Neither a specific grappling point nor any complex feedback control is required in our mechanism compared to the rigid methods, and its controllability is better than the flexible ones. ii) an implementation of the caging that uses a highly integrated deployable end-effector including only one actuator, without the need for initial explosive devices. iii) a novel contact detumbling method based on the friction to consume the residual angular momentum of the target around three axes, without the need for high-precision control and complex mechanisms.

2. Approach and concept

2.1 Target

Recent ADR studies have considered the targets sized ≥ 10 cm, because a majority of these objects are well observed and tracked in the LEO (Meyer et al. 2010). Malfunctioned satellites have been selected as the target in most of the aforementioned projects. A collision of these satellites will not only cause the loss of spacecraft, but also create a cloud of debris. Weight, probabilities of collision and altitudes should be taken into consideration to select a target (White et al. 2014). However, what

this paper cares most is the concept of the capture mechanism instead of the target selection. Thus, a simplified cubic satellite is assumed here to be the target. The kinematic parameters of its main body are listed in Table 1.

2.2 Caging

A geometrical closure is created around an object by the grippers such that the object is caged (Rimon et al. 1999). This technique effectively avoids the free-floating object being pushed away during the capturing. The caging-based grasp can be achieved only by the geometrical information of the robot and object, instead of the complex mechanical analysis of the precise grasp depending on contact friction and elasticity. The 3D multifingered caging (Makita et al. 2008) is conducted in this research (Fig. 1). To evaluate the geometrical closure of the caged target, a condition called object closure (Wang et al. 2002) is used. In the case that the object closure is formed, an object is movable but cannot escape from a geometrical closure of the fingers/grippers. The necessary and sufficient condition for the 3D multifingered caging can be expressed as follows.

$$(1) \quad C_{\text{free_obj}} \neq \emptyset$$

$$(2) \quad C_{\text{free_obj}} \cap C_{\text{free_inf}} = \emptyset$$

where $C_{\text{free_obj}}$ denotes the free space where the object can move without interference, $C_{\text{free_inf}}$ denotes the free space where a point at infinity is included.

2.3 Tumbling of debris

According to the conservation of momentum, the motion of debris can be formulated as follows.

$$(3) \quad \begin{cases} I_x \ddot{\alpha}_x - I_{xy} \ddot{\alpha}_y - I_{xz} \ddot{\alpha}_z + (I_z - I_y) \omega_y \omega_z - I_{yz} (\omega_y^2 - \omega_z^2) - I_{xz} \omega_x \omega_y + I_{xy} \omega_x \omega_z = 0 \\ I_y \ddot{\alpha}_y - I_{xy} \ddot{\alpha}_x - I_{yz} \ddot{\alpha}_z + (I_z - I_x) \omega_x \omega_z - I_{xz} (\omega_x^2 - \omega_z^2) - I_{xy} \omega_y \omega_z + I_{yz} \omega_x \omega_y = 0 \\ I_z \ddot{\alpha}_z - I_{xz} \ddot{\alpha}_x - I_{yz} \ddot{\alpha}_y + (I_y - I_x) \omega_x \omega_y - I_{xy} (\omega_y^2 - \omega_z^2) - I_{yz} \omega_x \omega_z + I_{xz} \omega_y \omega_z = 0 \end{cases}$$

where ω_x , ω_y and ω_z denote the tumbling rates around the roll, pitch and yaw axes in the target frame respectively, I_x , I_y , I_z , I_{xy} , I_{yz} and I_{xz} denote the elements of the inertia matrix. Space debris is generally tumbling due to its residual angular momentum from Eq. (3), thus increasing the difficulty for the capture. Compared to non-tumbling targets, capturing their counterparts involves

much more complicated dynamic interaction among the target, servicer satellite and manipulator. The tumbling also makes great trouble for guidance of the manipulator to rendezvous and capture the target in a safe and secure manner. Namely, more high-precision tracking and complex control algorithms are in demand for capturing the tumbling targets.

2.4 Conceptual design

In an effort to capture the tumbling target in a simple manner, we propose a novel ADR system including a satellite, a manipulator and a deployable capture mechanism, as shown in Fig. 2. The capturing device, comprised of a deployable end-effector and a contact detumbling mechanism, has the characteristics of compaction and simplicity. It is also reusable and can be launched easily. These factors are all described in greater detail below. Once the capture has been accomplished after tracking, the satellite de-orbits and jettisons the debris.

3. Mechanism design of deployable end-effector

The end-effector is mainly composed of three subsystems, i.e. the capture, transmission and actuation. The novelty of this study is to endow the mechanism with a deployable function. Fig. 3a and Fig. 3b show the 3D model of the end-effector in the folded configuration and deployed configuration respectively, which is also a partially pantograph mechanism based on our previous study (Li et al. 2018). The specifications of the end-effector are shown in Table 2.

3.1 Capture subsystem

The function of the capture subsystem is to capture the target securely, namely, to form the caging-based grasp by closing the grippers after their deployment. The capture subsystem consists of two main devices: the grippers and hold-downs.

The overall design of the grippers gets the idea from the umbrella in our daily life. The minimum number of the grippers is three to have enough contact points needed to keep a steady fixation of the object. Nonetheless, considering the interference of the mechanical structure, weight and symmetry, six grippers can ensure better robustness. As shown in Fig. 4a, an offset between the gripper and line through the centrosymmetry center guarantees a more compact mechanical structure. In addition, this

arrangement results in a laminated effect of the closed gripper tips, which facilitates forming the caging closure, as shown in Fig. 4b.

As shown in Fig. 5a, the gripper is composed of the constant-torque spring hinges, carbon fiber tubes and connection assemblies. The application of the constant-torque spring hinges rather than motors brings three merits: i) the weight reduction of the grippers. ii) a deployable function of the mechanism. iii) the omission of complex control strategies. Besides, the tubes made of carbon fibers rather than metal contribute to the weight reduction. To keep the gripper folded during the space transport, a simple hold-down consisting of a flexible rope and a locating part fixed on the palm is developed. Unlike initiating explosive devices, there are two knots on both ends of the flexible rope, one is fixed on the ending tube and the other is restrained by the locating part. The rope goes through holes on the gripper. When it's time to deploy the gripper, it will first be rotated to a specific position where the second knot can go through a locating hole on the locating part, as shown in Fig. 5b. Then, the gripper will be released and deployed under the action of the constant-torque spring hinges.

As shown in Fig. 6a and Fig. 6b, key components in the hinge are the drum, spring coil and roller. From Fig. 6c, only the common tangent line segment of the drum and roller is the valid deformation area, where the elastic forces form the resultant force F_r . Thanks to the invariance of the valid deformation area during the rotation of brackets, the resultant force F_r and torque arm (length of the common tangent line segment) are almost constant, and the output torque is almost constant. Particularly, the latch mechanism, including plug screws, spiral springs and locating pins, is embedded in the hinge, as shown in Fig. 6d. Once the bracket reaches the expected position, the locating pin will stick into the locating hole under the pressure of the spiral spring to lock the whole mechanism. Moreover, to meet the energy-saving requirement, all the above mechanisms except the springs and standard components are made of the magnesium alloy with high strength and low density. To simplify the design procedure, adoption of the constant-torque spring makes the torque exerted on each joint be constant. Only half of the variables should be adjusted compared to volute spiral springs (Wang et al. 2016).

3.2 Transmission subsystem

Gears are one of the most effective means available to transmit rotary motion from one shaft to another. Three gear pairs mainly constitute the transmission subsystem, which implements six grippers' simultaneous motion with only one actuator, as shown in Fig. 7a. As the transmission is quite important for the capture, the transmission subsystem is protected by the designed protection covers from Fig. 7b.

In the first-stage internal gear pair, the pinion is mounted on the output of the actuation subsystem through a key joint. Bevel gears are employed to transmit the rotary motion between two perpendicular shafts in the second stage and third stage. To realize the compaction, the second-stage wheel with a large central hole connects with the first-stage wheel. The second-stage wheel meshes with six centrosymmetrical pinions, dividing a single power into six parts according to the speed ratio. The second-stage pinions are assembled on the third-stage pinion shafts through key joints correspondingly. Likewise, six third-stage wheels drive six grippers through corresponding shafts. Moreover, a group of angular contact bearings is utilized to support the combination of the first-stage wheel and second-stage wheel. Other shafts are supported by their corresponding connection assemblies, bearings, and bearing blocks installed on the palm.

3.3 Actuation subsystem

As shown in Fig. 8, the modular actuation subsystem consists of a brushless DC motor, a harmonic reducer, a torque sensor, a magnetic encoder, an optical encoder, a fail-safe brake and so on. The motor stator is fixed inside the assembly housing mechanism of the actuation subsystem, while the motor rotor drives the wave generator of the harmonic reducer through a shaft. In case of an outage, the fail-safe brake is assembled on the same shaft as well. The circular spline of the harmonic reducer is attached to the assembly housing mechanism, and the flex spline drives the output connection assembly. Compared to other reducers, the harmonic reducer is employed here to enhance the load ability to a great extent. Above all, the actuation subsystem is mounted on the palm through assembly connection mechanisms.

To enhance the safety and reliability of the on-orbit activity, the feedback control of the end-effector is required. Therefore, a variety of sensors are utilized in the actuation subsystem, as shown in Table 3. Torque information is measured by two full-bridges, which consists of eight gauges to compensate the temperature influence. Combining the information fusion acquired by the position sensors (Dang et al. 2009) with the speed ratio in the transmission subsystem, configuration of the grippers can be observed accurately. Two current sensors mounted on the circuit board are utilized here to ensure the accuracy of motor torque.

4. Optimal design of the grippers

Apparently, a larger envelope volume and lighter weight of the deployed grippers are needed for the capture. Hence, an optimal design of the grippers based on the kinematic synthesis is conducted.

4.1 Kinematic Synthesis

As shown in Fig. 9a, there are two frames established here, the reference frame and base frame. $A_1, B_1, C_1, D_1, E_1, F_1, G_1, H_1$ denote the coordinates on the gripper in the closed configuration after being deployed, while $A_2, B_2, C_2, D_2, E_2, F_2, G_2, H_2$ denote the coordinates on the gripper in the completely deployed configuration, O_1 denotes the common coordinate. The reference frame is above the base frame, where the axis X is collinear with the symmetrical center of the grippers. The base frame rotates α clockwise to the reference frame. Particularly, α is denoted as α_1 and α_2 in the deployed configuration and closed configuration respectively.

First, let us define the dimensions as: $l_0=O_1A_1=O_1A_2$, $l_1=A_1B_1=A_2B_2$, $l_2=B_1C_1=B_2C_2$, $l_3=C_1D_1=C_2D_2$, $l_4=D_1E_1=D_2E_2$, $l_5=E_1F_1=E_2F_2$, $l_6=F_1G_1=F_2G_2$, $l_7=G_1H_1=G_2H_2$. Coordinates of A, B, C, D, E, F, G and H in the reference frame can be formulated with the given $l_0 \sim l_7$ and $\beta_1 \sim \beta_6$. The matrix P_r denoting the coordinates in the reference frame can be written as follows:

$$(4) \quad P_r = \begin{bmatrix} P_{Xr} \\ P_{Yr} \end{bmatrix} = \begin{bmatrix} A_{Xr} & B_{Xr} & \cdots & H_{Xr} \\ A_{Yr} & B_{Yr} & \cdots & H_{Yr} \end{bmatrix}_{2 \times 8}$$

Similarly, the coordinates in the base frame are denoted by the matrix P_{base} . According to the transformation principle of coordinates, the following formulation can be derived as:

$$(5) \quad P_{\text{base}} = \begin{bmatrix} P_{x\text{base}} \\ P_{y\text{base}} \end{bmatrix} = \begin{bmatrix} \cos \alpha & \sin \alpha \\ -\sin \alpha & \cos \alpha \end{bmatrix} P_r + T$$

where

$$(6) \quad T = \begin{bmatrix} 0 & 0 & \dots & 0 \\ l_0 \sin \alpha + R & l_0 \sin \alpha + R & \dots & l_0 \sin \alpha + R \end{bmatrix}_{2 \times 8}$$

4.2 Optimization of the grippers

1) Objective function formulation

The objective function consists of the envelope volume of the deployed grippers and the length of the tubes. To approximate the envelope volume of the completely deployed grippers, the cumulative sum of seven circular truncated cone volumes is employed, as shown in Fig. 9b. According to the kinematic synthesis given in Eq. (5), the first objective function can be formulated as:

$$(7) \quad f_1(x) = \sum_{i=1}^7 \frac{\pi}{3} [P_{\text{base}}(1, i+1) - P_{\text{base}}(1, i)] \times [P_{\text{base}}^2(2, i) + P_{\text{base}}^2(2, i+1) + P_{\text{base}}(2, i)P_{\text{base}}(2, i+1)]$$

The distances between two adjacent hinges should be taken into consideration to meet the lightweight requirement. Taking account of the simplicity and universality, a number of the distances are set to be equal to each other, $l_2=l_3=l_4=l_5=l_6$. So the second objective function can be expressed as follows:

$$(8) \quad f_2(x) = l_0 + l_1 + 5l_2 + l_7$$

The method of multiplication and division is adopted empirically in this multi-objective optimal problem for relative simplicity. At last, the objective function can be expressed in term of fraction as:

$$(9) \quad f(x) = f_2(x) / f_1(x)$$

2) Design variables

To ensure the simplicity and universality of the constant-torque hinges, all the included angles between two adjacent tubes are set to be equal to each other, $\beta_1=\beta_2=\beta_3=\beta_4=\beta_5=\beta_6$. While R ($=468.47\text{mm}$) is already designed in the transmission subsystem, the vector of design variables is:

$$(10) \quad \mathbf{x} = [l_0 \quad l_1 \quad l_2 \quad l_7 \quad \beta_1 \quad \alpha_1 \quad \alpha_2]^T$$

The lower bounds and upper bounds of the design variables are chosen based on empirical parameters as follows:

$$(11) \quad \mathbf{x} \in \{[80, 100], [380, 390], [490, 500], [515, 525], [155, 165], [0, 5], [40, 60]\}^T.$$

Likewise, the initial values of the design variables are set as:

$$(12) \quad \mathbf{x}_0 = [90 \quad 385 \quad 496 \quad 523 \quad 160 \quad 5 \quad 47.5]^T.$$

3) Constraint function

To ensure the comfortable appearance of the end-effector and the noninterference of the folded gripper tips, the distances between two adjacent hinges should be constrained as:

$$(13) \quad l_2 - l_1 \leq 90$$

$$(14) \quad l_7 - l_2 \leq 30$$

An appropriate coordinate range of the deployed gripper tips is employed to ensure a secure grasp as:

$$(15) \quad 1700 \leq H_{Y_{\text{base}}}(\alpha = \alpha_1) \leq 2250$$

The conditions given in Eq. (1) and Eq. (2) are required to form the 3D multifingered caging-based grasp as well. Since the orientation can be left out for caging a sphere, an object with the maximal inscribed sphere radius of 500mm ($=R_{\text{obj}}$) is employed. From Fig. 10a, the following is sufficient to prevent the sphere from escaping through the gap between the closed gripper tips:

$$(16) \quad d_{\text{tip}} < R_{\text{obj}}$$

where d_{tip} is the distance between two adjacent gripper tips. Combining the orthohexagonal arrangement of the grippers with the kinematic synthesis result given in Eq. (5), Eq. (16) can be formulated as:

$$(17) \quad H_{Y_{\text{base}}}(\alpha = \alpha_2) < 500$$

An enough envelope of the closed grippers is necessary, thus

$$(18) \quad -200 < H_{Y_{base}}(\alpha = \alpha_2) < 500$$

From Fig. 10b, the following is sufficient to prevent the sphere from escaping through the side gap between the closed grippers:

$$(19) \quad \max[P_{Y_{base}}(\alpha = \alpha_2)] = L < 2R_{obj} = 1000$$

where L is the gap width depicted in Fig. 10b.

4) Optimization results

Owing to the nonlinearity of the objective and constraint function, the sequential unconstrained minimization technique (SUMT) is adopted in this research according to trial assignments. Fig. 11 shows the iterative results of the objective function. It can be noticed that the numerical computation for the optimization process is converged after 121 iterations, despite the appearance due to the large scale of the axis Y and the minimal allowable tolerance defined as 1×10^{-10} . Table 4 shows the optimization results, whose approximate values will be employed in fabricating the grippers. The weight of the end-effector plummets from 182.7 Kg to 170.1 Kg after the optimization, while the envelope volume soars from 22.0 m³ to 29.2 m³.

5. Design of detumbling mechanism

5.1 Detumbling Torque

During the detumbling process, feedback forces and torque will be transmitted to the manipulator. The detumbling procedure aims to reduce the impact that may damage the manipulator. To enhance the effectiveness and to enlarge the detumbling force, a contact method without high-precision control and complex mechanisms is proposed. Triaxial detumbling torque is employed to consume the residual angular momentum, as shown in Fig. 12. Generally, the axis Z_3 is set to be the direction, around which the largest angular momentum of the debris is exerted. The detumbling torque in their respective local frames is:

$$(20) \quad \begin{cases} {}^1\mathbf{M}_1 = [0, 0, m_1]^T \\ {}^2\mathbf{M}_2 = [0, 0, m_2]^T \\ {}^3\mathbf{M}_3 = [0, 0, m_3]^T \end{cases}$$

where m_i ($i=1, 2, 3$) denotes the magnitude of the torque. The detumbling torque exerted on the end-effector around the roll axis

in the frame \mathbf{O}_3 can be expressed as:

$$(21) \quad \mathbf{M}_{\text{end}} = {}^1_3R^1 \mathbf{M}_1 + {}^1_2R^2 \mathbf{M}_2 + {}^3 \mathbf{M}_3$$

where i_jR denotes the rotation matrix of the frame \mathbf{O}_j with respect to the frame \mathbf{O}_i , therefore

$$(22) \quad \mathbf{M}_{\text{end}} = \begin{bmatrix} \sin \alpha_2 \sin \theta_2 m_1 \\ (\cos \alpha_2 \sin \alpha_1 + \cos \alpha_1 \sin \alpha_2 \cos \theta_2) m_1 - \sin \alpha_2 m_2 \\ (\cos \alpha_1 \cos \alpha_2 - \sin \alpha_1 \sin \alpha_2 \cos \theta_2) m_1 + \cos \alpha_2 m_2 + m_3 \end{bmatrix}$$

where θ_i ($i=1, 2$) and α_i ($i=1, 2$) denote the joint variable and link twist in the D-H convention. Detumbling torque is exerted around the three axes from Eq. (22), and does negative work around the three axes at the same time to slowdown the target.

Considering the singularity and workspace of mechanisms, α_1 and α_2 are set to be 90° and 45° in our previous study, respectively (Sun et al. 2018).

The detumbling torque is provided by two revolute friction disks with central holes along their axes for the feed-through of cables, such as the data bus of sensors and system power in the end-effector. The detumbling torque can be expressed based on the friction as:

$$(23) \quad m = \frac{2(r_2^3 - r_1^3)\mu F}{3(r_2^2 - r_1^2)}$$

where μ denotes the friction coefficient between two friction disks, r_2 and r_1 denote the outer radius and inner radius of the friction area respectively, F is assumed to be a uniformly distributed normal force. External normal pressure may decrease to a small value in the later stage during the detumbling, which may lower the efficiency. Hence, normal preload pressure is adopted here to ensure the effectiveness.

5.2 Design of the damper

So far, design of the mechanism can be carried out to generate the detumbling torque. The detumbling mechanism mainly consists of three dampers located along three axes to provide the aforementioned torque. Each damper (Fig. 13a) is mainly

composed of two revolute friction disks, two slip rings, six spiral springs, two thin wall bearings, housing mechanisms and so on. Compared to the friction cylinders, the friction disks bring three merits: i) the reduction of the axial dimension. ii) the enlargement of the contact area. iii) the improvement of the heat dissipation. Although a central hole is located along the axis of the damper, continuous triaxial rotation will result in the cable interwinding to damage the electronics. Therefore, two slip rings are embedded in each damper to transmit the electricity for the end-effector. These two slip rings in different sizes are used to avoid the signal interference. The outer slip ring supplies the power while the inner slip ring transmits the sensor signals. The stator of the outer slip ring connects to the housing mechanism and the stator of the inner slip ring. To realize the compaction, both the rotators of two slip rings are mounted on the hollow shaft supported by a group of angular contact bearings. The upper friction disk is also installed on the hollow shaft to ensure the rotation and limit the axial motion of the friction disk, while the lower friction disk is attached to the housing mechanism. Six centrosymmetrical springs serve as the preload pressure to provide the detumbling torque, on condition that the external normal pressure is too small to slowdown the target effectively during the later stage. To enhance the abrasive resistance, thermal stability and reliability of the friction disks, the ceramic matrix composite is plated on their contact areas. Moreover, assembly mechanisms are also designed to connect the dampers as shown in Fig. 13b, considering the compaction and noninterference during the detumbling. The specifications of the detumbling mechanism are listed in Table 5.

6. Simulation verification

Ground experiments and simulations are alternatives to verify the compliance of the mechanism to the requirements. Owing to the high cost and complexity of the ground testbed, only the simulation in the virtual software is conducted primarily in this study. The dynamic simulation software ADAMS is employed to verify the performance of the proposed mechanism.

6.1 Capturing

The capturing scenario is depicted in Fig. 14. Various simulations are conducted to obtain the capturing tolerance as listed

in Table 6, which is large enough to ensure a secure grasp. In stage 1, the end-effector approaches the object through manipulator during the cruise. In stage 2, the folded grippers are rotated to the specific position, where the hold-downs will be out of action. In stage 3, the grippers are deployed under the action of the constant-torque spring hinges. In stage 4, the grippers are already deployed. In stage 5, the deployed grippers are opened to the “ready to capture” configuration allowing a maximum capture range for the target dimensions and detection. In stage 6, the end-effector snares the object. In stage 7, the deployed grippers are closed to capture the object and ensure a caging-based grasp. In stage 8, the failsafe brake locks the mechanism to maintain the grasp. Above all, all the commands come either from the ground control or on-board avionics of the hosting satellite.

6.2 Detumbling

After grasping the tumbling debris, the residual angular momentum actuates the detumbling mechanism to generate the detumbling torque. To better verify the performance of the detumbling mechanism, the manipulator is set to be motionless. The preload forces generated by the centrosymmetrical springs are chosen to be 2N of both the damper 1 and damper 2. The axis Z_3 in the frame \mathbf{O}_3 is assumed here to be collinear with the axis Z in the target frame, namely, the main detumbling direction, and the preload force of the damper 3 is 5N. Apparently, external normal forces will be exerted on each damper as shown in Fig. 15. The external normal forces larger than preload forces play a crucial role in the earlier stage during the detumbling. After that, the gap between them narrows. Fig. 16 shows the generated detumbling torque, which relates to not only the friction coefficient but also the rotary velocity. All the torque almost plummets to zero at last. As is clear from Fig. 17, the kinetic energy of the target gradually declines over the detumbling. Fig. 18 illustrates the tumbling rates around the three axes in the target frame. At time $t=4854s$ the tumbling rates almost vanish, in spite of the marginal fluctuation caused by dynamic inequalities.

Study results of the aforementioned methods are listed in Table 7. The tumbling rates decrease slightly but still remain by means of the brush-type contactor and the cushion-type damper. The tethered space robot and thruster plume impingement suffer from complex control strategies and mechanisms, in spite of their faster detumbling. The electrostatic method and

electromagnetic method are much more time-consuming than others. Our method cuts out complex control strategies and mechanisms. Furthermore, the tumbling vanishes at the end and the performance on saving time is better than the majority of other methods.

7. Conclusions

This paper has presented the concept of a novel deployable end-effector and detumbling mechanism for capturing tumbling space debris. The multifingered caging was brought into capturing the object without precise positioning in the deployable end-effector. Three highly integrated subsystems of the end-effector for the capture, transmission and actuation are presented in detail respectively. An optimal design of the grippers, based on the caging grasp and kinematic synthesis, leads to the mechanism weight of 170.1 Kg compared to the original weight of 182.7 Kg, along with the envelope volume soaring from 22.0 m³ to 29.2 m³. Besides, a contact detumbling mechanism consisting of three dampers is introduced to consume the residual angular momentum of the debris around the three axes. Considering the signal interference and cable interwinding, each damper based on the friction is developed with two embedded slip rings for the simplicity and reliability. Additionally, the technical advancement of our proposed mechanism is demonstrated by the simulations.

Acknowledgement

This research has been financially supported by the National Key R&D Program of China (Grant No.2017YF1300400), the Major Research Plan of the National Natural Science Foundation of China (Grant No.61690210), the Foundation for Innovative Research Groups of the National Natural Science Foundation of China (Grant No.51521003) and the National Natural Science Foundation of China (Grant No.51775129). The authors would like to thank Yuhong Su, Yi Ren, He Yin and Shipeng Cui for their assistance in language proofreading.

References

Aghili, F. 2012. A prediction and motion-planning scheme for visually guided robotic capturing of free-floating tumbling

objects with uncertain dynamics. *IEEE Trans. Robot.* 28(3):634-649. <https://doi.org/10.1109/TRO.2011.2179581>

Araromi, O. A., Gavrilovich, I., Shintake, J., Rosset, S., Richard, M., Gass, V., et al. 2015. Rollable multisegment dielectric elastomer minimum energy structures for a deployable microsatellite gripper. *IEEE/ASME Trans. Mechatron.* 20(1): 438-446. <https://doi.org/10.1109/TMECH.2014.2329367>

Bennett, T., Stevenson, D., Hogan, E., and Schaub, H. 2015. Prospects and challenges of touchless electrostatic detumbling of small bodies. *Adv. Space Res.* 56(3): 557-568. <https://doi.org/10.1016/j.asr.2015.03.037>

Bischof, B. 2003. ROGER-Robotic geostationary orbit restorer. In *Proc. of 54th International Astronautical Congress of the International Astronautical Federation, the International Academy of Astronautics, and the International Institute of Space Law*, September 2003.

Dang, J., Ni, F., Gu, Y., Jin, M., and Liu, H. 2009. A highly integrated and flexible joint test system based on DSP/FPGA-FPGA. In *Proc. 2009 IEEE International Conference on Robotics and Biomimetics*, May 2009. pp. 1877-1882.

Debus, T. J., and Dougherty, S. P. 2009. Overview and performance of the front-end robotics enabling near-term demonstration (FREND) robotic arm. In *Proc. AIAA Infotech@ Aerospace Conference*, Seattle, April 2009. pp. 1-12.

Estrada, M. A., Jiang, H., Noll, B., Hawkes, E. W., Pavone, M., and Cutkosky M. R. 2017. Force and moment constraints of a curved surface gripper and wrist for assistive free flyers. In *Proc. 2017 IEEE International Conference on Robotics and Automation (ICRA)*, May 2017. pp. 2824-2830.

Gomez, N. O., and Walker, S. J. I. 2017. Guidance, navigation, and control for the eddy brake method. *J. Guid. Control Dyn.* 40(1): 52-68. <https://doi.org/10.2514/1.G002081>

Hausmann, G., Wieser, M., Haarmann, R., Brito, A., Meyer, J., Jäkel, S., et al. 2015. E. Deorbit mission: OHB debris

removal concepts. In Proc. of the 13th Symposium on Advanced Space Technologies in Robotics and Automation (ASTRA'2015), May 2015, Noordwijk. pp. 3-4.

Hirano, D., Kato, H., and Tanishima, N. 2017. Caging-based grasp with flexible manipulation for robust capture of a free-floating target. In Proc. 2017 IEEE International Conference on Robotics and Automation (ICRA), May 2017. pp. 5480-5486.

Hirano, D., Nagaoka, K., and Yoshida, K. 2013. Design of underactuated hand for caging-based grasping of free-flying object. in Proc. 2013 IEEE/SICE International Symposium on System Integration (SII), December 2013, pp. 436-442.

Huang, P. F., Zhang, F., Meng, Z. J., and Liu, Z. 2016. Adaptive control for space debris removal with uncertain kinematics, dynamics and states. *Acta Astronaut.* 128: 416-430. <https://doi.org/10.1016/j.actaastro.2016.07.043>

Kitamura, S., Hayakawa, Y., and Kawamoto, S. 2014. A reorbiter for large GEO debris objects using ion beam irradiation. *Acta Astronaut.* 94(2):725-735. <https://doi.org/10.1016/j.actaastro.2013.07.037>

Kumar, R., and Sedwick, R. J. 2013. Despinning orbital debris before docking using laser ablation. *J. Spacecr. Rocket.* 52(4): 1129-1134. <https://doi.org/10.2514/1.A33183>

Liou, J. C., and Johnson, N. L. 2006. Risks in Space from Orbiting Debris. *Sci.* 311: 340-341. <https://doi.org/10.1126/science.1121337>.

Li, X., Zhang, Y, Sun, K., and Liu, H. 2018. A Deployable End-effector with Caging-Based Grasp Capability for Capturing Free-Floating Objects. in Proc. IEEE International Conference on Mechatronics and Automation (ICMA), August 2018, pp. 455-460.

Makita, S., and Maeda, Y. 2008. 3D multifingered caging: Basic formulation and planning. In Proc. 2008 IEEE/RSJ International Conference on Intelligent Robots and Systems, October 2008, pp. 2697-2702.

- Matunaga, S., Kanzawa, T., and Ohkami, Y. 2001. Rotational motion-damper for the capture of an uncontrolled floating satellite. *Control Eng. Pract.* 9(2): 199-205. [https://doi.org/10.1016/S0967-0661\(00\)00098-8](https://doi.org/10.1016/S0967-0661(00)00098-8)
- Mcguire, J. R., and Yura, J. 2006. Advances in the analysis and design of constant-torque springs. In *Proc. of the 30th Aerospace Mechanism Symposium*, NASA Goddard Space Flight Center, 2006, pp. 205-220.
- Meyer, J., Scheper, M., Mato, J. V., and Letty, R. L. 2010. Design and development of a tentacles based clamping capture mechanism for active debris removal. In *Proc. of the International Symposium on Artificial Intelligence, Robotics and Automation in Space (i-SAIRAS)*, 2010, pp. 244-251.
- Nakajima, Y., Mitani, S., Tani, H., Murakami, N., Yamamoto, T., and Yamanaka, K. 2016. Detumbling space debris via thruster plume impingement. In *Proc. AIAA/AAS Astrodynamics Specialist Conference, AIAA SPACE Forum*, Long Beach: AIAA, September 2016. pp. 1–20.
- Nishida, S. I., and Kawamoto, S. 2011. Strategy for capturing of a tumbling space debris. *Acta Astronaut.* 68(1): 113-120. <https://doi.org/10.1016/j.actaastro.2010.06.045>
- Qi, X., Huang H., Miao, Z., Li, B., and Deng, Z. 2017. Design and Mobility Analysis of Large Deployable Mechanisms Based on Plane-Symmetric Bricard Linkage. *J. Mech. Des.* 139(2): 022302. <https://doi.org/10.1115/1.4035003>
- Qi, X., Huang H., Li, B., and Deng, Z. 2016. A Large Ring Deployable Mechanism for Space Satellite Antenna. *Aerosp. Sci. Technol.* 58: 498-510. <https://doi.org/10.1016/j.ast.2016.09.014>
- Reintsema, D., Thaeter, J., Rathke, A., Naumann, W., Rank, P., and Sommer, J. 2010. DEOS—the German robotics approach to secure and de-orbit malfunctioned satellites from low earth orbits. In *Proc. of the International Symposium on Artificial Intelligence, Robotics and Automation in Space (i-SAIRAS)*, 2010. pp. 244-251.

- Rimon, E., and Blake, A. 1999. Caging planar bodies by one-parameter two fingered gripping systems. *Int. J. Robot. Res.* 18(3): 299-318. <https://doi.org/10.1177/02783649922066222>
- Shan, M., Guo, J., and Gill, E. 2016. Review and comparison of active space debris capturing and removal methods. *Prog. Aerosp. Sci.* 80: 18-32. <https://doi.org/10.1016/j.paerosci.2015.11.001>
- Sun, K., Wang, Z., and Liu, H. 2018. Triaxial Contact Detumbling of Large-scale Space Debris. In *Proc. 2018 IEEE Advanced Information Technology, Electronic and Automation Control Conference*, August 2018. (in press)
- Wang, M., Zhou, X., Du, S. H., and Wang, Z. 2016. Study on Deployable Structure Synchronization Technology Based on Torque Control Method. *Manned Spacefl.* 22(1): 88-92. (in Chinese)
- Wang, Z. D., and Kumar, V. 2002. Object closure and manipulation by multiple cooperating mobile robots. In *Proc. 2002 IEEE International Conference on Robotics and Automation (ICRA)*, April 2002, pp. 394-399.
- White, A. E., and Lewis, H. G. 2014. The many futures of active debris removal. *Acta Astronaut.* 95:189-197. <https://doi.org/10.1016/j.actaastro.2013.11.009>
- Wormnes, K., Letty, R. L., Summerer, L., Schonenborg, R., Dubois-Matra, O., Luraschi, E., et al. 2013. ESA technologies for space debris remediation. In *Proc. of the 6th IAASS Conference: Safety is Not an Option*, Montreal, August 2013. pp. 3-4.
- Zhang, B., Liang, B., Wang, Z., Mi, Y., Zhang, Y., and Chen, Z. 2017. Coordinated stabilization for space robot after capturing a noncooperative target with large inertia. *Acta Astronaut.* 134:75-84. <https://doi.org/10.1016/j.actaastro.2017.01.041>

Table 1. Kinematic parameters of the Target

| Parameter | Value | Unit |
|--------------------------------------|--------|-------------------|
| Weight | 1500 | Kg |
| Main body size along X direction | 1000 | mm |
| Main Body size along Y direction | 1000 | mm |
| Main Body size along Z direction | 1000 | mm |
| Inertia moment I_{xx} | 187.50 | Kg m ² |
| Inertia moment I_{yy} | 250.05 | Kg m ² |
| Inertia moment I_{zz} | 312.54 | Kg m ² |
| Tumbling rate around pitch direction | 4 | °/s |
| Tumbling rate around yaw direction | 5 | °/s |
| Tumbling rate around roll direction | 10 | °/s |

Table 2. Specifications of the end-effector

| Parameter | Value | Unit |
|----------------|--------------------------------|------|
| Weight | 171 | Kg |
| Length | 670 (Folded), 2500 (Deployed) | mm |
| Diameter | 1224 (Folded), 4430 (Deployed) | mm |
| Deploying time | 10 | s |
| Capturing time | 10 | s |

Draft

Table 3. Configurations of sensors

| Name | Quantity | Principle | Measured data |
|------------------|----------|--------------------|----------------------------|
| Torque Sensor | 1 | Strain Gauge | Output torque |
| Magnetic Encoder | 1 | Magnetic Induction | Absolute position of motor |
| Hall Sensor | 3 | Hall Effect | Relative position of motor |
| Optical Encoder | 1 | Grating | Output absolute position |
| Current Sensor | 2 | Resistance Drop | Drive current |

Draft

Table 4. Optimization results

| Parameter | Value | Parameter | Value |
|-----------|---------|------------|----------|
| l_0 | 88.394 | β_1 | 164.589° |
| l_1 | 388.14 | α_1 | 4.568° |
| l_2 | 487.62 | α_2 | 53.403° |
| l_7 | 516.852 | | |

Draft

Table 5. Specifications of the detumbling mechanism

| Parameter | Value | Unit |
|------------------------|-------|------|
| Size along X direction | 211 | mm |
| Size along Y direction | 183 | mm |
| Size along Z direction | 405 | mm |
| Weight | 14 | Kg |

Draft

Table 6. Capturing tolerance of the end-effector

| Tolerance | Value | Unit |
|--------------------------------|-------|------|
| Displacement along X direction | 730 | mm |
| Displacement along Y direction | 1300 | mm |
| Displacement along Z direction | 1405 | mm |

Draft

Table 7. Comparison with other detumbling methods

| Methods | Target mass (Kg) | Detumbling time (s) |
|---|------------------|---------------------|
| Brush-type contactor (Nishida et al. 2011) | 500 | \ |
| Cushion-type damper (Matunaga et al. 2001) | 2000 | \ |
| Tethered space robot (Huang et al. 2016) | 675 | 108 |
| Thruster plume impingement (Nakajima et al. 2016) | 2000 | 5000 |
| Electrostatic method (Bennett et al. 2015) | 1000 | 612000 |
| Electromagnetic method (Gomez et al. 2017) | 2154 | 129600 |
| Our method | 1500 | 4854 |

Fig. 1. 3D multifingered caging.

Fig. 2. Composition of the ADR system.

Fig. 3. 3D model of the end-effector. (a) Folded configuration; (b) Deployed configuration.

Fig. 4. Arrangement of the grippers. (a) Offset arrangement; (b) Laminated effect.

Fig. 5. Capture subsystem. (a) Gripper and hold-down; (b) Locating hole.

Fig. 6. Constant-torque spring hinge. (a) Compressed configuration; (b) Released configuration; (c) Schematic; (d) Section view.

Fig. 7. Transmission subsystem. (a) Multistage gears; (b) Protection cover.

Fig. 8. Actuation subsystem.

Fig. 9. Schematic diagram of the grippers. (a) Gripper with frames; (b) Section view of circular truncated cones.

Fig. 10. Schematic views of the caging-based grasp. (a) At the gripper tip; (b) At the cross section with the maximal gap.

Fig. 11. Iterative results of the objective function.

Fig. 12. Spatial position of the detumbling torque.

Fig. 13. 3D model of the detumbling mechanism. (a) Damper; (b) Connected dampers.

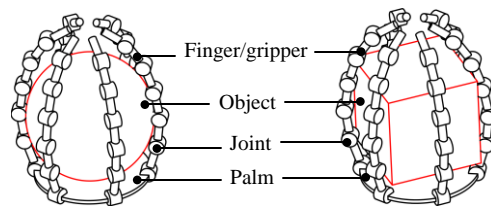
Fig. 14. Schematic of the capture scenario.

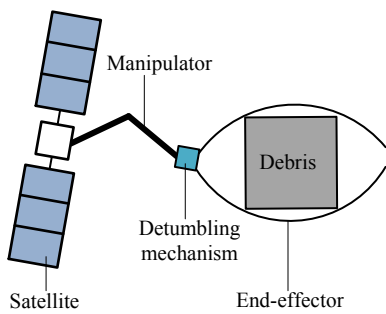
Fig. 15. External normal forces exerted on each damper.

Fig. 16. Detumbling torque generated by each damper.

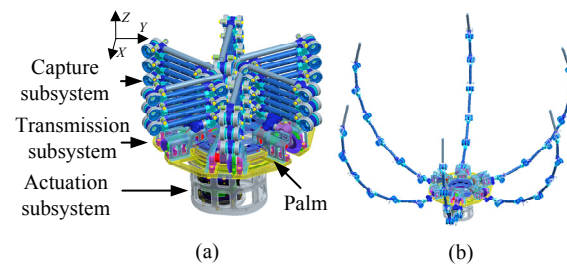
Fig. 17. Kinetic energy of the target.

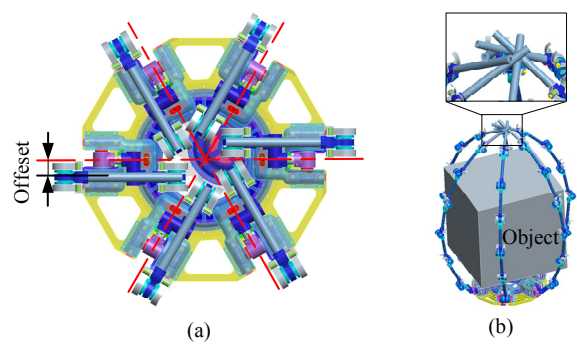
Fig. 18. Tumbling rates of the target.



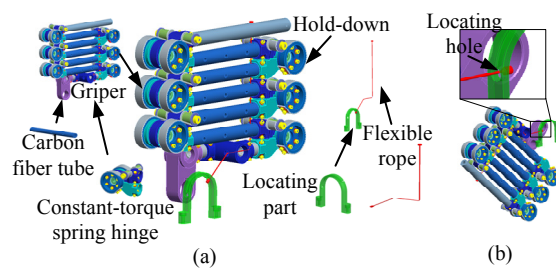


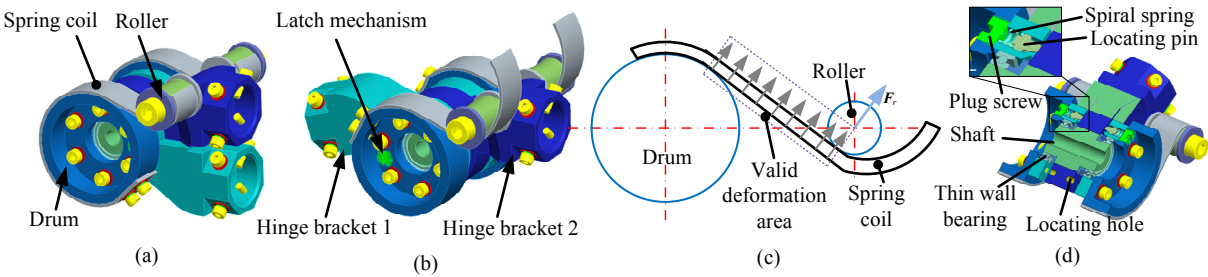
Draft



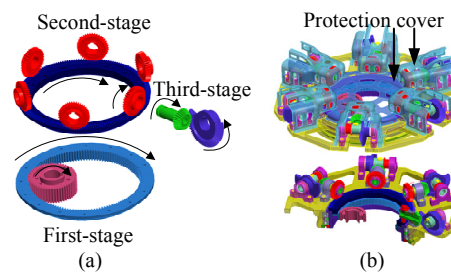


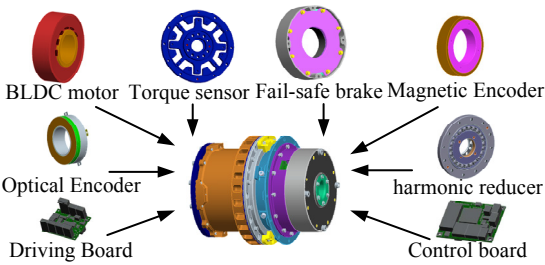
Draft

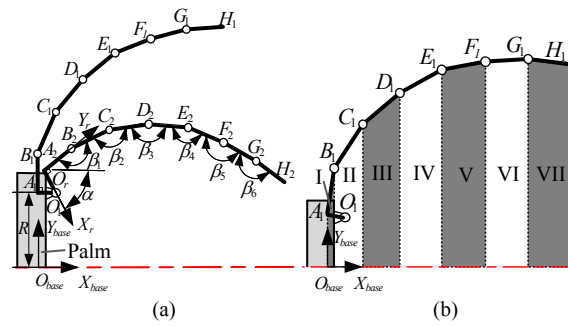


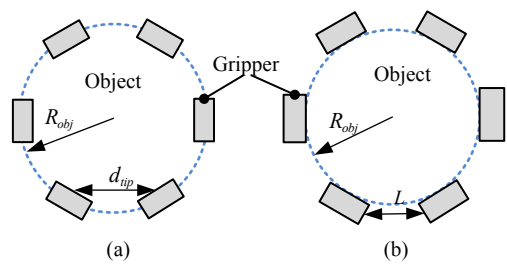


Draft

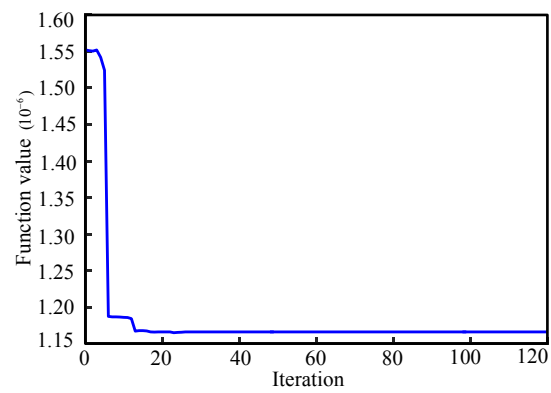




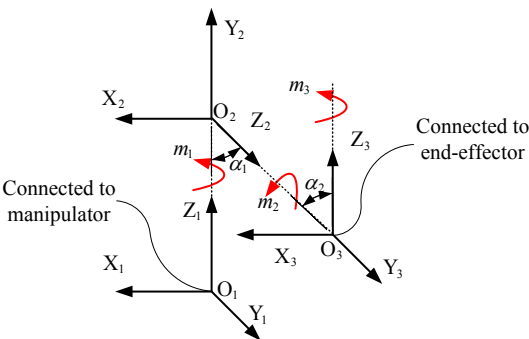


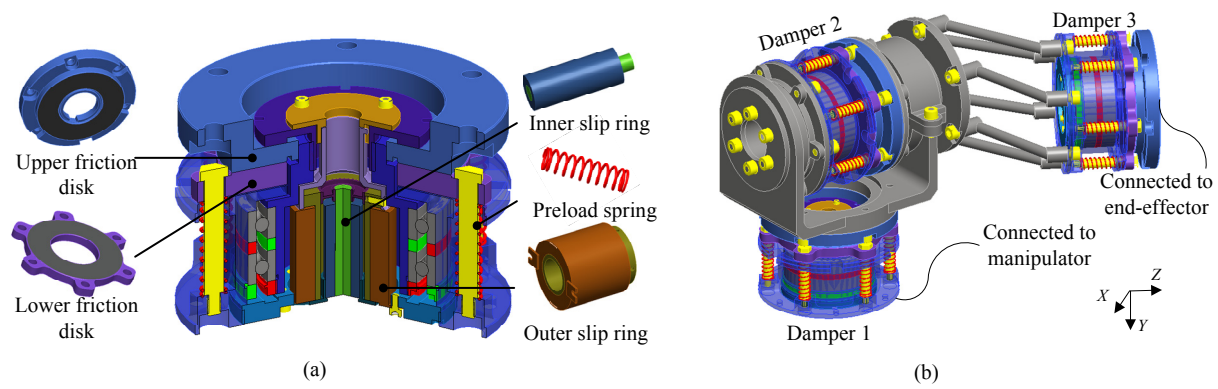


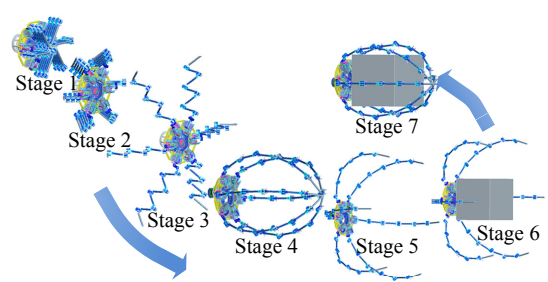
Draft



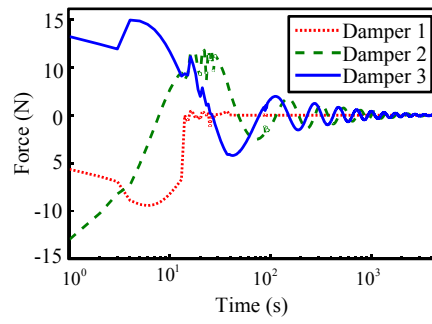
Draft



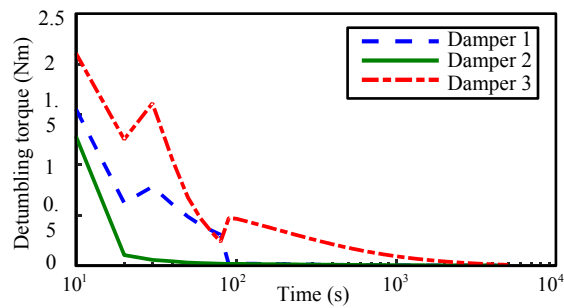




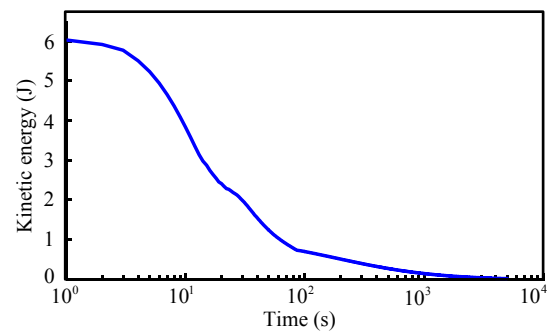
Draft



Draft



Draft



Draft

